Cryo-electron microscopy structures of human oligosaccharyltransferase complexes OST-A and OST-B

Originally published in:
Science 366(6471), https://doi.org/10.1126/science.aaz3505

Funding acknowledgement:
173709 - GlycoSTART: Structure and function of eukaryotic oligosaccharyltransferase (SNF)

Cryo-EM structures of human oligosaccharyltransferase complexes OST-A and OST-B

Ana S. Ramírez[1†], Julia Kowal[1†] and Kaspar P. Locher[1]*

[1] Institute of Molecular Biology and Biophysics, Eidgenössische Technische Hochschule (ETH), CH-8093 Zürich, Switzerland.

*Correspondence to: locher@mol.biol.ethz.ch

† Both authors contributed equally to this work.

Abstract: Oligosaccharyltransferase (OST) catalyzes the transfer of a high-mannose glycan onto secretory proteins in the endoplasmic reticulum. Mammals express two distinct OST complexes that act in a co-translational (OST-A) or post-translocational (OST-B) manner. We here present high-resolution cryo-EM structures of human OST-A and OST-B. While revealing similar overall architectures, structural differences in the catalytic subunits STT3A and STT3B facilitate contacts to distinct OST subunits DC2 or MAGT1. In OST-A, interactions with TMEM258 and STT3A allow ribophorin-I to form a 4-helix bundle that can bind to a translating ribosome, whereas the equivalent region is disordered in OST-B. We observed an acceptor peptide and dolichylphosphate (DolP) bound to STT3B, but only DolP in STT3A, suggesting distinct affinities of the two OST complexes for acceptor protein substrates.

One Sentence Summary: Structure of the human oligosaccharyltransferase complexes OST-A and OST-B

N-glycosylation is one of the most prevalent post-translational modifications of secretory proteins(*1*, *2*). It is estimated that more than 10% of human proteins carry *N*-glycans(*3*), which are essential for intracellular processes such as protein folding and trafficking, and for extracellular recognition and signaling(*1*, *2*). The process is initiated in the endoplasmic reticulum (ER) with the transfer of the pre-assembled, high-mannose oligosaccharide $GlcNac_2$-Man_9-Glc_3 from a dolichyl-pyrophosphate carrier to asparagine residues in the glycosylation sequon Asn-X-Thr/Ser(*4*). This reaction is catalyzed by oligosaccharyltransferase (OST), a multi-subunit complex located in the ER membrane(*1*, *2*, *5*). Unlike yeast, human cells contain two distinct OST complexes, OST-A and OST-B(*2*), and their combined functions result in a glycoproteome roughly ten times larger than that of yeast(*6*). The OST-A and OST-B complexes share six subunits (ribophorin-I, ribophorin-II, OST48, TMEM258, DAD1 and OST4)(*7*–*9*), but feature distinct paralogous catalytic subunits, STT3A or STT3B(*10*). In addition, OST-A contains the adapter protein DC2 that mediates the association with the protein translocation channel Sec61(*11*, *12*). When bound to translating, membrane-associated ribosomes and the translocon-associated protein complex (TRAP), a super-complex is formed that couples the synthesis, translocation into the ER, and *N*-glycosylation of secretory proteins(*11*, *12*). In contrast, OST-B does not contain DC2 but instead contains either MAGT1 or TUSC3 (OST3 or OST6 in yeast, respectively)(*13*, *14*), two paralogous redox chaperones. These allow OST-B to catalyze post-translocational processing of acceptor sites even near folded protein elements or formed disulfide bridges (*14*–*16*).

The recently published high-resolution cryo-EM structures of yeast OST provided insight into the architecture of multimeric OST systems (*12*, *17*, *18*). Furthermore, a medium-resolution cryo-EM structure visualized how OST-A associates with the translocon and the ribosome. However, the structural basis of the distinct functions of human OST-A and OST-B requires high-resolution structures of both complexes. In addition, whereas bacterial and archaeal single-subunit OST enzymes including PglB and AglB, have been visualized in the presence of substrates(*19*–*21*), no structures of eukaryotic OST complexes have been determined in substrate-bound states. To tackle these questions, we separately purified human OST-A and OST-B from HEK cells by expressing affinity-tagged versions of DC2 (for OST-A) or MAGT1 (for OST-B) (Fig. S1). The purified OST complexes were homogeneous and functional, as shown by an *in vitro* glycosylation assay using a fluorescently labeled peptide and a synthetic, lipid-linked oligosaccharide (LLO) analog containing a disaccharide ($GlcNAc_2$) moiety (Fig. 1). Intriguingly, we found that glycan transfer catalyzed by OST-B was faster than by OST-A. Furthermore, the reactions proceeded more efficiently when a chemo-enzymatically extended LLO analog carrying five additional mannoses ($GlcNAc_2Man_5$)(*22*, *23*) was transferred, suggesting that the mannose units increase the affinity of both human OST complexes for the LLO.

Single-particle cryo-EM analysis of the purified OST-A and OST-B complexes resulted in three-dimensional reconstructions with overall resolutions of 3.5 Å in both cases (Fig. 1). The local resolution of the transmembrane domains and of the central parts of the luminal regions was substantially better and allowed unambiguous building of atomic models (Fig. S2-5). Despite the low sequence similarity between human and yeast OST subunits (between 30-50%, Table S1), the overall architectures of OST-A and OST-B resemble that of the yeast enzyme ($RMSD_{OST\text{-}A\text{-}yOST}$: 2.75 Å for 1660 Cα atoms / $RMSD_{OST\text{-}B\text{-}yOST}$: 1.99 Å for 1730 Cα atoms) (*17*, *18*). Thus, similar subcomplexes can be identified: Subcomplex I consists of ribophorin-I and TMEM258 and is identical in OST-A and OST-B. Subcomplex II is distinct in the two OST versions: In OST-A, it consists of OST4, the catalytic STT3A subunit and the translocon adaptor protein DC2. In OST-B,

it features OST4, the catalytic STT3B subunit and the redox chaperone MAGT1 (Fig. S6). Although Western blots demonstrate that full length MAGT1 was present in our OST-B preparations (Fig. 2A), the EM map only revealed clear densities for TM2-4, which showed a remarkable structural similarity to DC2 (Fig. 2B). Finally, subcomplex III consists of DAD1, OST48 and ribophorin-II (Fig. S6). Human ribophorin II contains an N-terminal extension of about 300 residues compared to its yeast homolog SWP1. Whereas this region is highly flexible in OST-A, it is visible in the EM map of OST-B. This is likely due to interactions with a C-terminal extension of STT3B that is absent in STT3A. As a consequence of this stabilization, ribophorin II displays two main conformations in OST-B (Fig. S7 and Movie S1). In the transmembrane (TM) interfaces between the three subcomplexes, we observed several ordered phospholipids and digitonin molecules. Ordered *N*-glycans on the surface of OST were observed for the catalytic subunits STT3A (N537 and N548) and STT3B (N616, N627, and N641), and for ribophorin-I (N299) (Fig. S8-9).

Various additional proteins have been proposed to interact with mammalian OST. We found strong density consistent with a transmembrane helix and a short luminal stretch of malectin in close proximity to the TM domain of TMEM258 and the luminal domain of ribophorin-I. Western blot analysis of purified OST-A and OST-B complexes revealed a strong signal for full-length malectin in OST-B, but a lower signal in OST-A preparations, suggesting that malectin is bound in sub-stoichiometric amounts in OST-A (Fig. S10). While malectin was proposed to have a role in quality control during the folding of glycoproteins, its precise molecular mechanism remains to be clarified(*24*). The observation that malectin is bound and partially ordered illustrates that human OST complexes can serve as platforms for interactions that help modulate protein *N*-linked glycosylation by controlling attached glycans and the status of glyco-protein folding.

The remarkable similarity between human OST-A and OST-B (RMSD: 0.96 Å for 1715 Cα atoms) suggests that subtle structural differences are responsible for their specific subunit interactions and their distinct cellular functions. We noted two key differences: First, despite the similar arrangement of transmembrane helices TM10-13, there are differences in the protein surfaces where STT3A and STT3B interact with DC2 or MAGT1 (Fig. 2B). A detailed analysis revealed that neither could MAGT1 associate with STT3A, nor could DC2 associate with STT3B due to steric clashes (Fig. S11). As a consequence, only OST-A can interact with the translocon. The second structural difference is that even in the absence of bound ribosome, the C-terminal domain of ribophorin-I forms a cytoplasmic 4-helix bundle in OST-A. This bundle was found in contact with translating ribosome in a recent tomography study (*12*). In contrast, no such feature was visible in the EM of OST-B (Fig. 2C). To rule out that a truncation of ribophorin-I had occurred in our OST-B preparation, we conducted Western blot analysis using antibodies recognizing the C- or N-terminal regions of ribophorin-I. This revealed that full-length ribophorin-I was present in both OST complexes (Fig. 2D), suggesting that the C-terminal region of ribophorin-I is disordered in OST-B. Our high-resolution structures provide an explanation for this key difference: In OST-A, the first helix of the C-terminal region of ribophorin-I interacts with the cytoplasmic loop connecting TM1 and TM2 of TMEM258. Specifically, Glu470 of ribophorin-I forms a hydrogen bond with the side chain of Tyr46 of TMEM258, which is simultaneously involved in a cation–π interaction with its neighboring residue Lys45 (Fig. 2C). In contrast, such an interaction is absent in OST-B, where TM1 of STT3B and TM2 of TMEM258 are tilted compared to their position in OST-A (Fig. 2E). Furthermore, the cytoplasmic, N-terminal

segment of STT3B is 56 residues longer than that of STT3A. Given that this region is in the immediate vicinity of the C-terminal region of ribophorin-I, it is more likely to interfere with the folding of the 4-helix bundle than the shorter segment of STT3A (Fig. 2C).

The catalytic subunits STT3A and STT3B form similar active sites. While previously reported structures of yeast OST were visualized in apo states(*17*, *18*), we observed well-defined density for two ligands bound to STT3B (Fig. 3a, Fig. S12). Furthermore, whereas TM9 and EL5 (connecting TM9 and TM10) were disordered in the yeast apo-OST structures, both adopted an "engaged" conformation in human OST-B, reminiscent of the conformational changes observed in bacterial PglB upon binding to substrates(*19*, *21*). The remarkable difference to PglB is that with the exception of divalent metal ions present in the purification buffers, no cofactors, substrates or substrate analogs were added to our OST-B preparations. The bound substrate analogs had thus been retained from the native cellular environment during purification, which suggests relatively high affinities. The density in the peptide binding pocket could be interpreted as an average of polypeptides containing an *N*-glycosylation sequon. As was observed in PglB, the polypeptide backbone formed a 180º turn (Fig. 1A, 3A), suggesting that only unfolded polypeptide regions can be processed by OST-B. The side chain of the +2 threonine is in close proximity to the conserved WWD motif, which has been demonstrated to be essential for sequon recognition(*25*). The side chain of the acceptor asparagine is located in a tunnel formed by the packing of EL5 against the ER-luminal domain of STT3B and is in close proximity of the catalytic Asp103 residue and of the side chain of Asn623 that is part of the conserved "DNNT loop" (Fig. 3B) (*19*, *21*, *26*). We further observed density consistent with a bound divalent metal ion in the active site (Fig. 3A) in the vicinity of conserved, negatively charged side chains including Asp103 as well as residues Asp167 and Glu169 of the DxE motif (*19*, *21*, *25*).

A hydrophobic groove formed by TM6 and TM11 is present on the surface of STT3B (Fig. 3C), similar to grooves observed in PglB and the apo-structures of yeast OST(*17–19*, *25*). In human OST-B, this groove contained well-defined density of a bound molecule featuring the characteristic shape of a polyprenyl chain, as well as strong density for a phosphate group in contact with the divalent ion and a conserved arginine side chain (Arg459). However, no density was visible for a second phosphate group or for ordered glycans, ruling out the possibility that a functional LLO containing a pyrophosphate group and a glycan was bound. We therefore interpreted the observed density as a bound dolichylphosphate (DolP) molecule. While surprising, DolP was recently shown to co-purify with the ER-localized O-mannosyltransferase complex PMT1-PMT2(*27*). In our OST-B structure, the phosphate group of bound DolP forms hydrogen bonds with Arg459, Arg383, and Trp283 of the STT3B subunit (Fig 3D). Arg459 is a conserved residue in OST enzymes that appears to stabilize the leaving group DolPP during the nucleophilic substitution reaction(*25*). We found that the guanidinium group of Arg459 was in hydrogen bonding distance with Glu403, a catalytic residue located within EL5, and shown to be essential for activity both in bacterial PglB and yeast OST(*17*, *28*).

In contrast to OST-B, no density for a bound peptide was observed in OST-A. However, density for a bound DolP molecule was clearly visible in the LLO-binding groove. The interactions of bound DolP with STT3A are very similar to those observed in STT3B, suggesting a conserved mechanism for LLO recognition in both complexes (Fig. 3D). Despite the absence of bound peptide, EL5 of STT3A was fully ordered and adopted a similar conformation as in STT3B (Fig. S12) demonstrating that DolP binding is sufficient for EL5 to adopt an engaged conformation.

This is notably different to bacterial PglB, where an equivalent conformational change requires the binding of both LLO and acceptor peptide (*19*, *21*). The absence of bound peptide in our OST-A structure suggests that OST-B has a significantly higher affinity for acceptor peptides.

Our structural observations correlate well with the distinct cellular functions of OST-A and OST-B: OST-A is responsible for processing of the majority of *N*-glycosylation sites. Due to its proximity to the translocon, it is exposed to the unfolded polypeptide sequences of all secretory proteins and therefore able to process even suboptimal sequons(*29*). In contrast, OST-B processes proteins that are already partially folded and may even contain disulfide bridges. This requires OST-B to have strongly increased affinity for glycosylation sequons compared to OST-A, which is in line with our structural observation that co-purified peptides were bound to the OST-B complex. Our finding that purified OST-A had a lower *in vitro* activity than OST-B is both intriguing and counterintuitive. The challenge of OST-A is to keep up with protein translation and translocation and prevent that protein folding in the ER removes target glycosylation sites. One would thus expect OST-A to be the faster enzyme than OST-B. The fact that the opposite is observed *in vitro* suggests the possibility that in the cell, interactions with the translocon and the translating ribosome may stimulate OST-A and thus increase its catalytic rate through, either through altered protein dynamics or by inducing conformational changes.

In conclusion, our results not only provide structural insight into substrate binding of eukaryotic OST complexes but also establish that the distinct functions of human OST-A and OST-B are based on structural differences of their catalytic subunits STT3A and STT3B, which result in interactions with distinct subunits and different affinities for acceptor peptides. Our results also provide a structural basis for the design of new inhibitors of *N*-glycosylation that modulate the maturation and activation of protein markers involved in tumor formation(*30*).

References

1. J. Breitling, M. Aebi, N-Linked Protein Glycosylation in the Endoplasmic Reticulum. *Cold Spring Harb. Perspect. Biol.* **5**, a013359–a013359 (2013).
2. N. Cherepanova, S. Shrimal, R. Gilmore, N-linked glycosylation and homeostasis of the endoplasmic reticulum. *Curr. Opin. Cell Biol.* **41**, 57–65 (2016).
3. U. Garg, L. D. Smith, R. Ganetzky, F. J. Reynoso, M. He, Congenital disorders of glycosylation. *Biomarkers Inborn Errors Metab.*, 343–360 (2017).
4. R. G. Spiro, Glycoproteins. *Adv. Protein Chem.* **27**, 349–467 (1973).
5. D. F. Zielinska, F. Gnad, J. R. Wiśniewski, M. Mann, Precision mapping of an in vivo N-glycoproteome reveals rigid topological and sequence constraints. *Cell*. **141**, 897–907 (2010).
6. M. Aebi, N-linked protein glycosylation in the ER. *Biochim. Biophys. Acta*. **1833**, 2430–7 (2013).
7. D. J. Kelleher, R. Gilmore, An evolving view of the eukaryotic oligosaccharyltransferase. *Glycobiology*. **16**, 47R-62R (2006).
8. A. Dumax-Vorzet, P. Roboti, S. High, OST4 is a subunit of the mammalian oligosaccharyltransferase required for efficient N-glycosylation. *J. Cell Sci.* **126**, 2595–606 (2013).
9. D. B. Graham *et al.*, TMEM258 is a component of the cligosaccharyltransferase complex controlling ER stress and intestinal inflammation. *Cell Rep.* **17**, 2955–2965 (2016).
10. D. J. Kelleher, D. Karaoglu, E. C. Mandon, R. Gilmore, Oligosaccharyltransferase isoforms that contain different catalytic STT3 subunits have distinct enzymatic properties. *Mol. Cell*. **12**, 101–111 (2003).
11. S. Shrimal, N. A. Cherepanova, R. Gilmore, DC2 and KCP2 mediate the interaction between the oligosaccharyltransferase and the ER translocon. *J. Cell Biol.* **216**, 3625–3638 (2017).
12. K. Braunger *et al.*, Structural basis for coupling protein transport and N-glycosylation at the mammalian endoplasmic reticulum. *Science*. **360**, 215–219 (2018).
13. B. L. Schulz *et al.*, Oxidoreductase activity of oligosaccharyltransferase subunits Ost3p and Ost6p defines site-specific glycosylation efficiency. *Proc. Natl. Acad. Sci. U. S. A.* **106**, 11061–11066 (2009).
14. N. A. Cherepanova, S. Shrimal, R. Gilmore, Oxidoreductase activity is necessary for N-glycosylation of cysteine-proximal acceptor sites in glycoproteins. *J. Cell Biol.* **206**, 525–539 (2014).
15. S. Shrimal, S. F. Trueman, R. Gilmore, Extreme C-terminal sites are posttranslocationally glycosylated by the STT3B isoform of the OST. *J. Cell Biol.* **201**, 81–95 (2013).
16. S. Shrimal *et al.*, Glycosylation of closely spaced acceptor sites in human glycoproteins. *J. Cell Sci.* **126**, 5513–23 (2013).
17. R. Wild *et al.*, Structure of the yeast oligosaccharyltransferase complex gives insight into eukaryotic N-glycosylation. *Science.* **359**, 545–550 (2018).
18. L. Bai, T. Wang, G. Zhao, A. Kovach, H. Li, The atomic structure of a eukaryotic oligosaccharyltransferase complex. *Nature*. **555**, 328–333 (2018).
19. M. Napiórkowska *et al.*, Molecular basis of lipid-linked oligosaccharide recognition and processing by bacterial oligosaccharyltransferase. *Nat. Struct. Mol. Biol.* **24**, 1100–1106 (2017).
20. S. Matsumoto, Y. Taguchi, A. Shimada, M. Igura, D. Kohda, Tethering an N-

glycosylation sequon-containing peptide creates a catalytically competent oligosaccharyltransferase complex. *Biochemistry*. **56**, 602–611 (2017).
21. M. Napiórkowska, J. Boilevin, T. Darbre, J.-L. Reymond, K. P. Locher, Structure of bacterial oligosaccharyltransferase PglB bound to a reactive LLO and an inhibitory peptide. *Sci. Rep.* **8**, 16297 (2018).
22. A. S. Ramírez *et al.*, Characterization of the single-subunit oligosaccharyltransferase STT3A from Trypanosoma brucei using synthetic peptides and lipid-linked oligosaccharide analogs. *Glycobiology*. **27**, 525–535 (2017).
23. A. S. Ramírez *et al.*, Chemo-enzymatic synthesis of lipid-linked GlcNAc2Man5 oligosaccharides using recombinant Alg1, Alg2 and Alg11 proteins. *Glycobiology*. **27**, 726–733 (2017).
24. K. Takeda, S. Y. Qin, N. Matsumoto, K. Yamamoto, Association of malectin with ribophorin i is crucial for attenuation of misfolded glycoprotein secretion. *Biochem. Biophys. Res. Commun.* **454**, 436–440 (2014).
25. C. Lizak, S. Gerber, S. Numao, M. Aebi, K. P. Locher, X-ray structure of a bacterial oligosaccharyltransferase. *Nature*. **474**, 350–355 (2011).
26. M. Igura *et al.*, Structure-guided identification of a new catalytic motif of oligosaccharyltransferase. *EMBO J.* **27**, 234–243 (2008).
27. L. Bai, A. Kovach, Q. You, A. Kenny, H. Li, Structure of the eukaryotic protein O-mannosyltransferase Pmt1−Pmt2 complex. *Nat. Struct. Mol. Biol.* **26**, 704–711 (2019).
28. S. Gerber *et al.*, Mechanism of Bacterial Oligosaccharyltransferase: In vitro quantification of seqon binding and catalysis. *J. Biol. Chem.* **288**, 8849–8861 (2013).
29. N. A. Cherepanova, S. V Venev, J. D. Leszyk, S. A. Shaffer, R. Gilmore, Quantitative glycoproteomics reveals new classes of STT3A- and STT3B-dependent N-glycosylation sites. *J. Cell Biol.* **218**, 2782–2796 (2019).
30. A. S. Puschnik *et al.*, A Small-Molecule Oligosaccharyltransferase Inhibitor with Pan-flaviviral Activity. *Cell Rep.* **21**, 3032–3039 (2017).
31. H. Schägger, Tricine–SDS-PAGE. Nat. Protoc. 1, 16–22 (2006).
32. D. Kohda, M. Yamada, M. Igura, J. Kamishikiryo, K. Maenaka, New oligosaccharyltransferase assay method. Glycobiology. 17, 1175–1182 (2007).
33. D. N. Mastronarde, Automated electron microscope tomography using robust prediction of specimen movements. J. Struct. Biol. 152, 36–51 (2005).
34. S. Q. Zheng et al., MotionCor2: Anisotropic correction of beam-induced motion for improved cryo-electron microscopy. Nat. Methods. 14 (2017), pp. 331–332.
35. K. Zhang, Gctf: Real-time CTF determination and correction. J. Struct. Biol. 193, 1–12 (2016).
36. J. Zivanov et al., New tools for automated high-resolution cryo-EM structure determination in RELION-3. Elife. 7 (2018).
37. A. Punjani, J. L. Rubinstein, D. J. Fleet, M. A. Brubaker, CryoSPARC: Algorithms for rapid unsupervised cryo-EM structure determination. Nat. Methods. 14, 290–296 (2017).
38. S. H. W. Scheres, S. Chen, Prevention of overfitting in cryo-EM structure determination. Nat. Methods. 9, 853–854 (2012).
39. E. F. Pettersen et al., UCSF Chimera - A visualization system for exploratory research and analysis. J. Comput. Chem. 25, 1605–1612 (2004).
40. T. D. Goddard et al., UCSF ChimeraX: Meeting modern challenges in visualization and analysis. Protein Sci. 27, 14–25 (2018).

41. P. Emsley, B. Lohkamp, W. G. Scott, K. Cowtan, Features and development of Coot. Acta Crystallogr. Sect. D Biol. Crystallogr. 66, 486–501 (2010).
42. N. W. Moriarty, R. W. Grosse-Kunstleve, P. D. Adams, Electronic ligand builder and optimization workbench (eLBOW): A tool for ligand coordinate and restraint generation. Acta Crystallogr. Sect. D Biol. Crystallogr. 65, 1074–1080 (2009).
43. P. D. Adams et al., PHENIX: A comprehensive Python-based system for macromolecular structure solution. Acta Crystallogr. Sect. D Biol. Crystallogr. 66, 213–221 (2010).
44. A. Brown et al., Tools for macromolecular model building and refinement into electron cryo-microscopy reconstructions. Acta Crystallogr. Sect. D Biol. Crystallogr. 71, 136–153 (2015).

Acknowledgments: We thank the staff at the Scientific Center for Optical and Electron Microscopy (ScopeM, ETH Zurich, Switzerland) for support during cryo-EM data collection; Jonas Zürcher for help with protein expression and cell culture work and Jérémy Boilevin and Jean-Louis Reymond for providing the LLO analog Farnesyl-Citronellyl-PP-$GlcNAc_2$. We thank Markus Aebi, Tamis Darbre and Jean-Louis Reymond for helpful discussions. **Funding:** This work was supported by the Swiss National Science Foundation (Transglyco and GlycoSTART Sinergia program funds to K.P.L.). **Author Contributions**: A.S.R. and K.P.L conceived the project and designed the experiments. A.S.R. performed cloning, preparation of stable cell lines, expression, purification and biochemical characterization of OST complexes. J.K. prepared cryo-EM grids, collected and processed EM data. A.S.R. built, refined and validated the structures with help of K.P.L. All the authors contributed to the writing of the manuscript. **Competing interests:** The authors declare no competing interests. **Data and materials availability:** Atomic coordinates of the OST-A and OST-B models were deposited in the RCSB Protein Data Bank (PDB) under accession number 6S7O for OST-A and 6S7T for OST-B. The three-dimensional cryo-EM maps were deposited in the Electron Microscopy Data Bank (EMDB) under accession numbers EMD-10110 for OST-A and EMD-10112 for OST-B. All other data is presented in the paper and supplementary materials.

Supplementary Materials:

Materials and Methods

Figures S1-S12

Tables S1-S2

Movie S1

References (31-44)

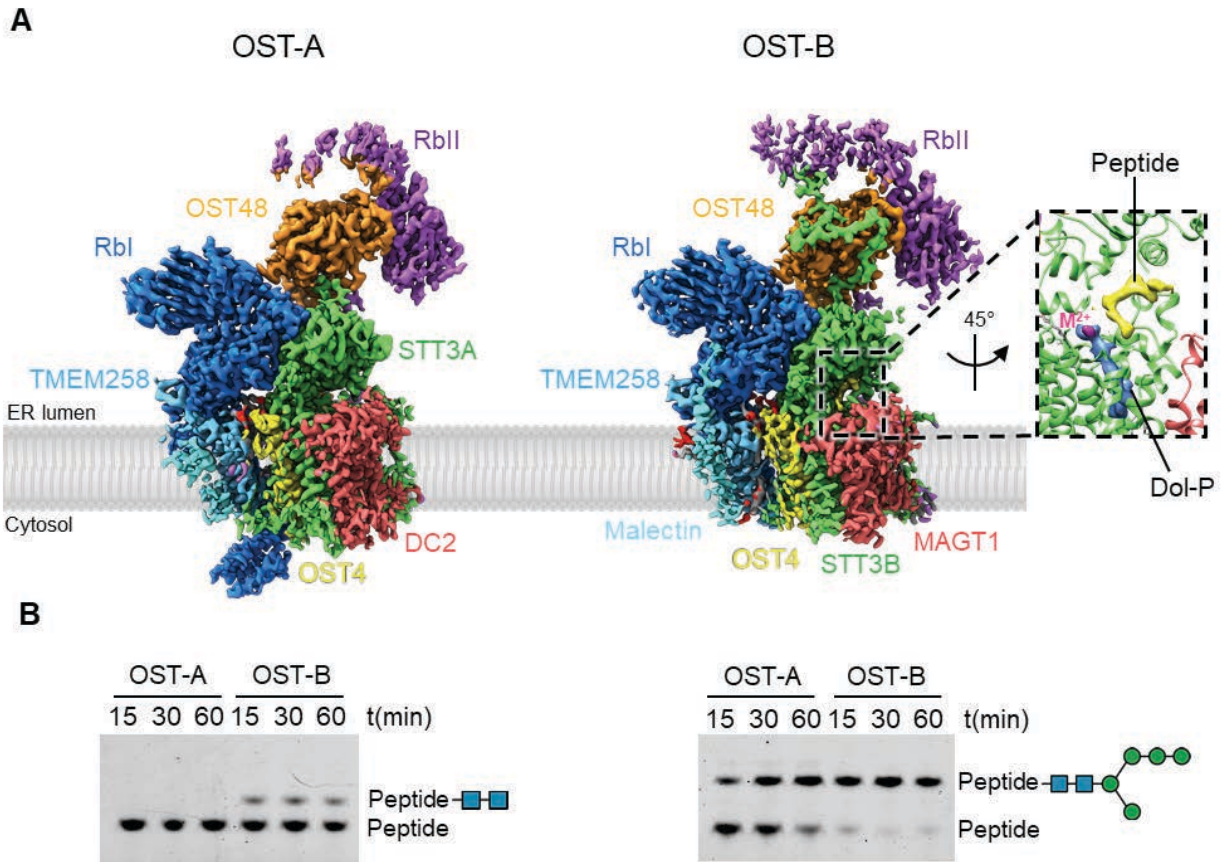

Fig.1. Biochemical and cryo-EM studies of the human OST complexes.

(A) Cryo-EM maps of OST-A (left) and OST-B (right) are shown and colored according to the subunits as indicated. Inset on the right shows the EM density for ligands bound to STT3-B. In this view, DAD1 is located behind STT3A and STT3B. **(B)** *In vitro* glycosylation assays with purified OST-A and OST-B complexes. Fluorescently labeled peptide TAMRA-GSGNSTVT was used as acceptor substrate and FarnesylCitronellyl-PP-$GlcNAc_2$ or FarnesylCitronellyl-PP-$GlcNAc_2Man_5$ as donor substrates. Glycosylated and non-glycosylated peptides were separated using SDS-PAGE Tricine gels.

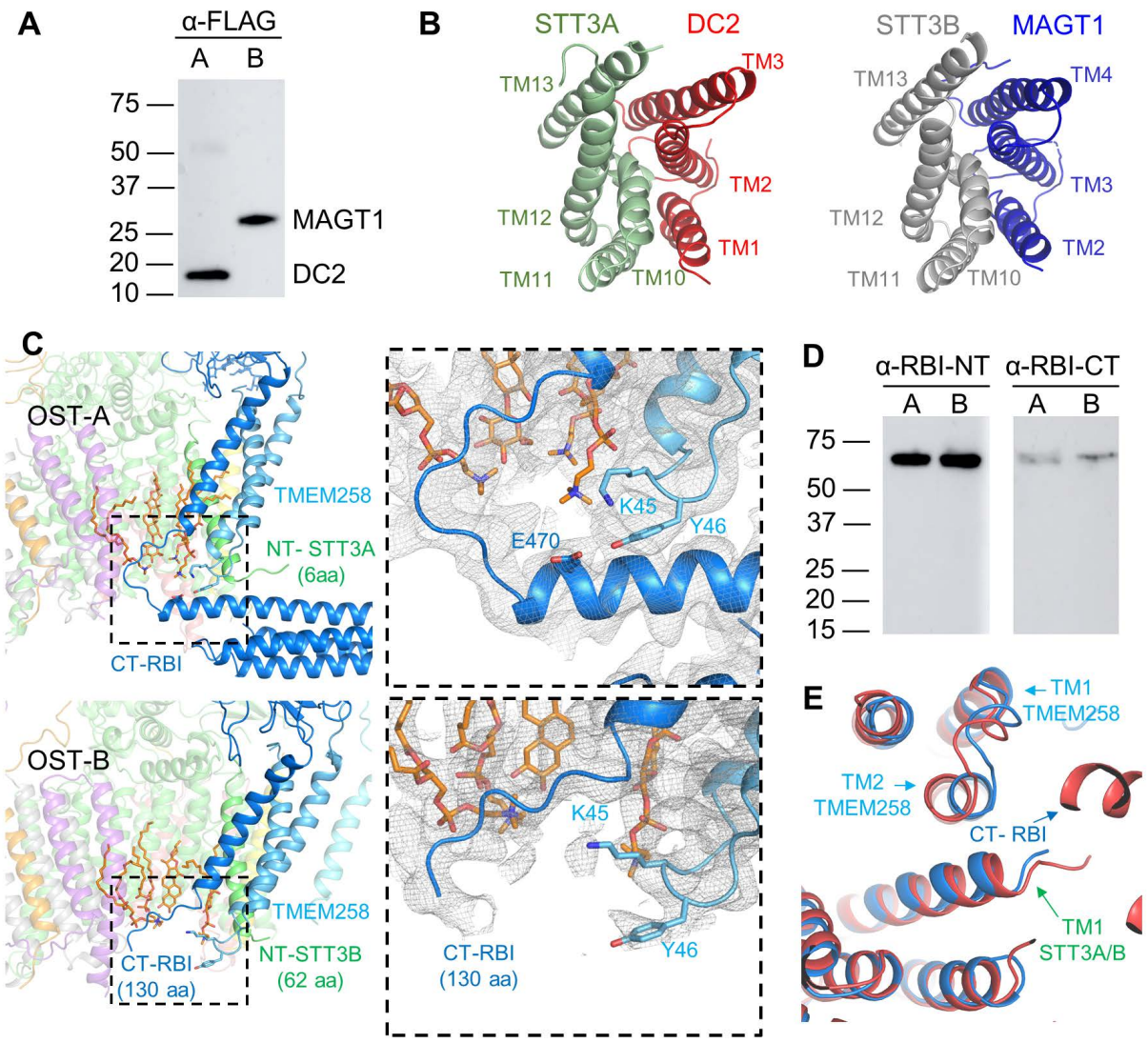

Figure 2: Interaction of STT3 paralogs with their neighbor subunits.
(A) Western blot analysis of purified OST-A and OST-B using anti-Flag antibody to detect Flag-tagged DC2 and MAGT1. **(B)** Cytosolic view onto the TM regions of STT3A and DC2 (left panel) and STT3B and MAGT1 (right panel). **(C)** Structural arrangement of ribophorin-I, TMEM258 and STT3 in OST-A (top) and OST-B (bottom). In the insets, closed-up views of the interaction between ribophorin-I and TMEM258. Residues involved in contacts are shown as sticks and labeled in single-letter code. EM density is shown as a gray mesh (Map levels: 4.0 σ, as defined by Pymol). Subunits are colored as in Fig 1. **(D)** Western blot analysis of purified OST-A and OST-B using antibodies against the N- or C-terminal regions (abbreviated as NT or CT) of ribophorin-I (RBI). **(E)** Cytoplasmic view onto the superimposed structures of OST-A (red cartoon) and OST-B (blue cartoon), focusing on the TM helices of ribophorin-I, TMEM258 and TM1 of the STT3 subunits.

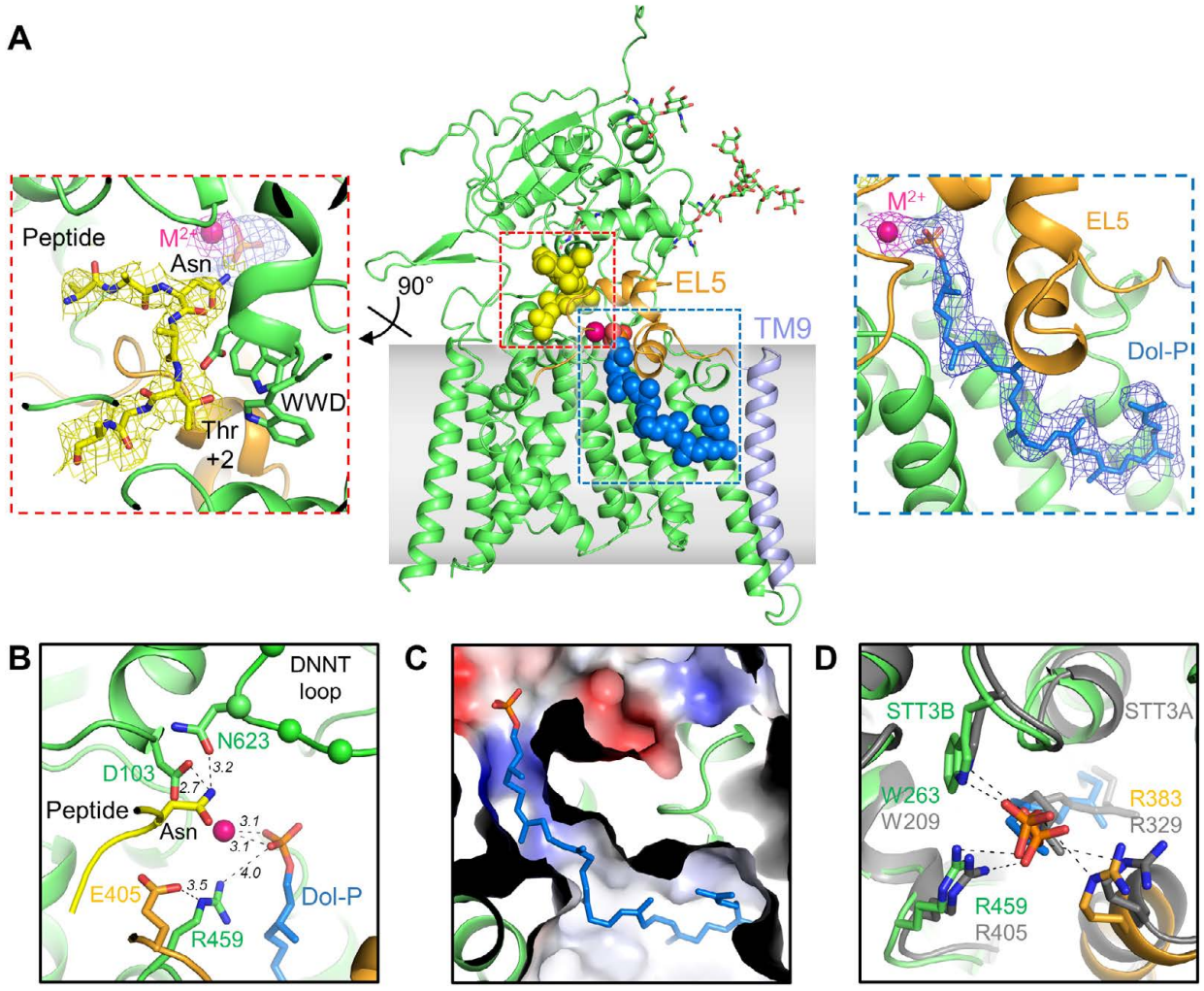

Figure 3: Active site of human OST.

(A) Structure of STT3B shown in cartoon representation. EL5 is colored orange and labeled. Transmembrane helix 9 (TM9) is colored light blue and labeled. Close-up of binding sites for bound peptide (left inset) and DolP (right inset). Bound peptide is shown as yellow sticks. Residues interacting with +2 position (WWD motif) are shown as sticks and labeled. DolP is shown as sticks with carbon atoms colored blue, while the divalent metal ion is shown as a pink sphere. The EM density covering bound substrates is shown as a mesh and colored according to substrate color (Map level: 5.0 σ, as defined by Pymol). **(B)** Close-up of active site of STT3B. Residues presumably involved in catalysis are shown as sticks and labeled. Bound peptide is shown as cartoon and the acceptor asparagine as sticks. Divalent ion is shown as a pink sphere. **(C)** Electrostatic surface potential of the LLO binding site, color-coded by electrostatic potential ranging from blue (most positive) to red (most negative). DolP is shown as in **A**. **(D)** View of the LLO binding site viewed from the ER lumen. STT3B residues interacting with the phosphate group of DolP are shown as sticks, colored as in (**A**) and labeled. A superposition of STT3A (gray) with bound DolP is shown.

Supplementary Materials for

Cryo-EM structures of human oligosaccharyltransferase complexes OST-A and OST-B

Ana S. Ramírez[1]†, Julia Kowal[1]† and Kaspar P. Locher[1]*
† Both authors contributed equally to this work.

Correspondence to: locher@mol.biol.ethz.ch

This PDF file includes:

Materials and Methods
Figs. S1 to S12
Tables S1 and S2
References 31 - 44
Captions for Movie S1

Other Supplementary Materials for this manuscript include the following:

Movie S1

Materials and Methods

Protein expression and purification of human OST complexes

Stable HEK293 cell lines enabling the tetracycline-inducible expression of DC2 or MAGT1 were generated using the Flp-In T-REx 293 Expression System (Thermo Fisher Scientific), following the manufacturer's guidelines. Both proteins carried an N-terminal Flag tag, for MAGT1 this was introduced after the predicted cleavage site of its signal peptide. The stable cell lines were grown and maintained in DMEM (Thermo Fisher Scientific) supplemented with 10% FBS and penicillin/streptomycin (Thermo Fisher Scientific) at 37 °C with 5% CO_2, under humidified conditions. Expression of DC2 or MAGT1 was induced with 1 μg/mL tetracycline (Sigma) for 24 h at 37 °C, followed by harvesting and washing with phosphate-buffered saline (Thermo Fisher Scientific). Cell pellets were frozen in liquid nitrogen and stored at –80°C.

For purification, cell pellets were thawed and resuspended in lysis buffer containing 50 mM HEPES, pH 7.5; 200 mM NaCl and 10% (w/v) glycerol, supplemented with cOmplete™, EDTA-free Protease Inhibitor Cocktail (Roche), and 0.5 mM phenyl- methanesulfonylfluoride (PMSF). Lysis was performed by dounce homogenization on ice, and all following steps were performed at 4 C. The membrane fraction was collected by high-speed centrifugation at 100,000 x g for 30 min, resuspended in solubilization buffer containing 50 mM HEPES, pH 7.5; 400mM NaCl; 5mM $MgCl_2$ and 10% (w/v) glycerol, and subsequently incubated with 1% (w/v) digitonin (Merck) for two hours. The supernatant was collected after high-speed centrifugation at 100,000 x g for 30 min and incubated with anti-Flag M2 affinity agarose gel (Sigma) for two hours. The gel was washed with solubilization buffer containing 0.1% (w/v) digitonin and subsequently with washing buffer containing 25 mM HEPES, pH 7.5; 150 mM NaCl; 3mM $MgCl_2$, 10% (w/v) glycerol and 0.1% (w/v) digitonin. OST complex was eluted with 0.4 mg/mL Flag peptide (Sigma) in washing buffer, concentrated and further purified by size exclusion chromatography using a TSKgel G4000SWXL column (Tosoh Bioscience) with a buffer containing 25 mM HEPES, pH 7.5; 150 mM NaCl; 2mM DTT and 3mM $MgCl_2$. The peak fractions were collected and used for cryo-EM and biochemical studies.

Detection of proteins by Western blot

Purified OST complexes were analyzed by Western blot to detect individual OST subunits using commercial antibodies. Anti-Ribophorin-I C-terminus (sc-48367) and anti-OST48 (sc-74408) were purchased from Santa Cruz Biotechnology. Anti-Ribophorin-I N-terminus (ab198508) and anti-malectin (ab97616) were purchased from Abcam. Anti-Flag (F3165) for the detection of tagged DC2 and MAGT1 was purchased from Sigma-Aldrich.

In vitro glycosylation assays

Reaction mixtures contained 0.5 μM purified OST-A or OST-B complex, 50μM FarnesylCitronellyl-PP-$GlcNAc_2$ or FarnesylCitronellyl-PP-$GlcNAc_2$-Man_5, 10 mM $MnCl_2$, and 10 μM of the fluorescently labeled peptide 5-TAMRA-GSGNSTVT. Reactions were incubated at 30 °C and analyzed Tricine SDS-PAGE consisting of a 16% resolving gel with 6 M urea, a 10% spacer gel, and a 4% stacking gel(*31, 32*).

Grid preparation and cryo-EM data acquisition

Cryo-EM grids were prepared using a Vitrobot Mark IV (FEI) with an environmental chamber set at 95% humidity and 4 °C. Aliquots of 4 µL of purified OST complexes at a protein concentration of 3.7 mg/mL (OST-B) and 5.5 mg/mL (OST-A), were placed onto Quantifoil carbon grids (R1.2/1.3, 300 mesh, copper) previously glow-discharged for 45 seconds with 25 mA using Pelco easiGlow 91000 Glow Discharge Cleaning System. Grids were blotted with filter paper (595 Filter paper from Schleicher & Schuell, diameter 55/20mm) for 3 – 3.5 s and flash-frozen in a mixture of liquid ethane and propane cooled by liquid nitrogen. Grids were imaged with a Titan Krios (FEI) electron microscope operated at 300 keV, equipped with a Gatan K2 Summit direct electron detector and Gatan Imaging Filter (GIF), with a slit width of 20 eV to remove inelastically scattered electrons. Movies were recorded semi-automatically with SerialEM(*33*) for OST-A or EPU software (Thermo Fisher Co.) for OST-B, in super-resolution counting mode with a defocus range of –0.5 to –2.5 µm and a super-resolution pixel size of 0.42 Å/pixel.

The final data set of OST-A was composed of 6,035 super-resolution movies (10,028 before manual inspection and filtering out poor micrographs) collected during three separate Titan Krios sessions. Each stack was exposed for 8 s with an exposure time of 0.2 s per frame with electron exposure of 6.0 e^-/pix/s, resulting in 40 frames per movie and a frame exposure rate of 1.7 $e^-/Å^2$. The final data set of OST-B was composed of 14,705 (17,262) super-resolution movies collected during two cryo-EM sessions. Movie stacks had identical exposure time, and frame number as OST-A data but electron exposure was 7-8 e^-/pix/s, resulting in a frame exposure rate of 2-2.3 $e^-/Å^2$. All stacks were gain-normalized, motion-corrected, dose-weighted and then binned 2-fold with MotionCor2(*34*). The defocus values were estimated on the non-dose-weighted micrographs with Gctf(*35*).

Cryo-EM data processing

Image processing of the two OST complexes was performed both in Relion 3.0(*36*) and CryoSPARC2(*37*). From the OST-A and OST-B dose-weighted micrographs, a total of 424,817 OST-A and 1,106,821 OST-B particles were picked with Gautomatch software (http://www.mrc-lmb.cam.ac.uk/kzhang/), respectively.

The OST-A particles were initially processed in 3 batches in Relion 3.0. After multiple rounds of 2D classifications, almost all particles (396,514) were correctly assigned to 2D classes. These particles were then 3D classified, using as reference a low-passed initial model obtained from the small data set (Dataset 1, Fig. S2) processed in CryoSPARC2 (*ab-initio* reconstruction). The particles from the best 3D classes containing 39.8%, 39% and 41% of particles, respectively, and showing fully intact molecules were unbinned, re-extracted with bigger box (486 x 486 pixels) and combined (156,950 particles from all 3 batches). Selected particles were then 3D auto-refined in Relion 3.0. The refinement was performed with a very soft mask covering the full density of the complex. The resolution of this map was 3.74 Å. For further processing steps, only the drift-corrected movie averages made of frames 1-7 (corresponding to the total dose of ~12 electrons per $Å^2$) were used. Refinement of these (1-7 frames) particles against the same starting model as before, using the three-dimensional auto-refine procedure continued with previously defined angles, and an angular sampling rate of 0.5 degree and local searches set up to 1.8 degrees, resulted

in a map at 3.58 Å resolution. At this point, the particles were applied for another 3D classification without alignments, with a soft mask covering the transmembrane region and the central part of the complex. After 3D classification, 135,697 particles from the best class were selected, regrouped and applied to series of 3D auto-refinements including per-particle CTF refinement routine and 3D refinement with soft mask excluding part of the four-helix bundle region of ribophorin-I and flexible part of ribophorin-II. The 3D reconstruction showed distinct features of the protein complex with an overall resolution of 3.51 Å (Map 1, with an automatically determined B-factor of −96.4 $Å^2$). This map was used for the initial model building. Then we performed 3D auto-refinements with mask excluding the flexible part of ribophorin-I and/or detergent belt around the transmembrane region. To further improve the map quality of the cytoplasmic region of ribophorin-I (Map 2 at 3.48 Å resolution, with an automatically determined B-factor of −77.8 $Å^2$) and the luminal region of ribophorin-II (Map 3 at 3.67 Å resolution, with an automatically determined B-factor of −80.8 $Å^2$). In parallel, the OST-A particles combined after 3D classification in Relion 3.0 were imported and processed in CryoSPARC2 where 2D classification, *ab initio* homogeneous 3D refinement (map at 3.79 Å resolution), and multireference heterogeneous refinement with two classes were performed.

The OST-B particles were initially processed in 2 batches in Relion 3.0. After many rounds of 2D classifications and selection, we obtained a final set of 904,054 particles which were 3D classified. The best 3D classes containing 197'852 (38%) and 134'058 (35%) of particles were re-extracted (384 x 384 box) without binning, joined and again 3D classified with two classes. After three-dimensional classification and selection, we obtained a final data set of 249'725 particles. The refinement in Relion 3.0 was performed with a very soft mask covering the full density of the complex. The resolution of this map was 3.70 Å. Subsequently, the series of 3D refinements including per-particle CTF refinement, Bayesian polishing and refinement with a soft mask without detergent belt was performed. Post-processing including masking and B-factor sharpening with automatically determined B-factor (−133.5 $Å^2$) resulted in a 3.54 Å-resolution map (Map 1), which was used for initial model building. Finally, we performed a 3D focused refinement in order to further improve the map quality of the STT3B and luminal region of ribophorin-II. 3D refinement resulted in a density map of 3.50 Å resolution (Map 2, with an automatically determined B-factor of −137.4 $Å^2$), showing distinct features of the focused domain.

As in the case of OST-A dataset, the previously classified OST-B particles (249'725) were exported to CryoSPARC2 where 2D classification, *ab initio* homogeneous 3D refinement (map at 4.0 Å resolution) and local 3D refinement with mask (map at 3.69 Å resolution) were performed. Multi-reference heterogeneous refinement resulted in three distinct 3D classes. Two out of three 3D classes, containing 43% and 38% of particles, respectively, reached near 4 Å resolutions and were used to visualize the conformational changes of the N-terminal distal domain of ribophorin-II. The particle stack contributing into 4 Å-resolution 3D map was used for further 3D Variability Analysis, which is a tool in CryoSPARC 2.9 for exploring both discrete and continuous heterogeneity in single particle cryo-EM data sets. In order to remove the signal coming from the micelle the mask without detergent belt made in Chimera was used. The simple linear "movies" of volumes were generated for 3 eigenvectors. Outputs were low-pass filtered during optimization to 5 Å and visualized with 3D Variability Display tool in CryoSPARC 2.9.

Post-processing in Relion included masking and sharpening with automatically determined B-factors. All resolutions were estimated by applying a soft mask around the protein complex

density and based on gold-standard Fourier shell correlation (FSC) 0.143 criterion(*38*). Relion 3.0 was used to calculate the local resolution maps. Figures containing EM maps were made using Chimera(*39*) and ChimeraX(*40*) software.

Model Building

For the generation of an initial model of OST-A, we used a post-processed map, at an overall resolution of 3.51 Å (Map 1, Fig. S2). Guided by the structure of yeast OST (PDB: 6EZN)*(20)*, we performed manual building and fitting where permitted by the map quality, using the software Coot(*41*). The EM density was of excellent quality in the transmembrane and luminal domain and allowed the unambiguous building of OST-A, except for the distal N-terminal domain (residues 1-367) of ribophorin-II. For the building of the C-terminal helix bundle of OST1, and part of the luminal domain of ribophorin-II (residues 368-506), we used a post-processed map of the full complex without the detergent belt at an overall resolution of 3.67 Å (Map 3, Fig. S2). In the C-terminal domain of ribophorin-I, we built and assigned side chains of the first helix, whereas the other three helices forming the bundle were built as a polyA model using low-pass filtered maps. For the building of OST-B, we dock the OST-A model in a post-processed map of the full OST-B complex at a resolution of 3.54 Å (Map 1, Fig. S4). Subsequently, we performed manual fitting of OST4, ribophorin-I, ribophorin-II, OST48, DAD1, and TMEM258. Guided by the structure of STT3A and DC2, we built STT3B and the C-terminal TM helices (TM2-TM4) of MAGT1. Further fitting of the luminal domain of ribophorin-II was performed using a post-processed map from a focused refinement of the luminal domains of OST-B at a resolution of 3.50 Å (Map 2, Fig. S4).

In OST-A, we observed continuous density for the building of five isoprenyl units of the lipid tail of DolP, whereas in OST-B, we could build eight isoprenyl units. The acceptor substrate observed in the active site of STT3B was modeled as a heptapeptide (poly-A model, except for the glycosylation sequon). Geometry restraints for DolP analogs, phospholipids, and digitonin molecules were generated in eLBOW(*42*).

The complete models were refined against the working maps in PHENIX(*43*) using real space refinement. The quality of the final models was analysed by MolProbity, and the refinement statistics are shown in Table S2. To validate the refinement, random shifts (mean value of 0.3 Å) were introduced into the coordinates of the final refined model using phenix.pdbtools, followed by real space refinement against the first unfiltered half-map (half-map 1, work). The overlay between the FSC curve of the model with random displacements refined against half-map1 versus half-map 1 (work) and the FSC curve of the same model versus half-map 2 (half2, against which it was not refined) indicated that no over-refinement took place(*44*) (Fig. S3, S5).

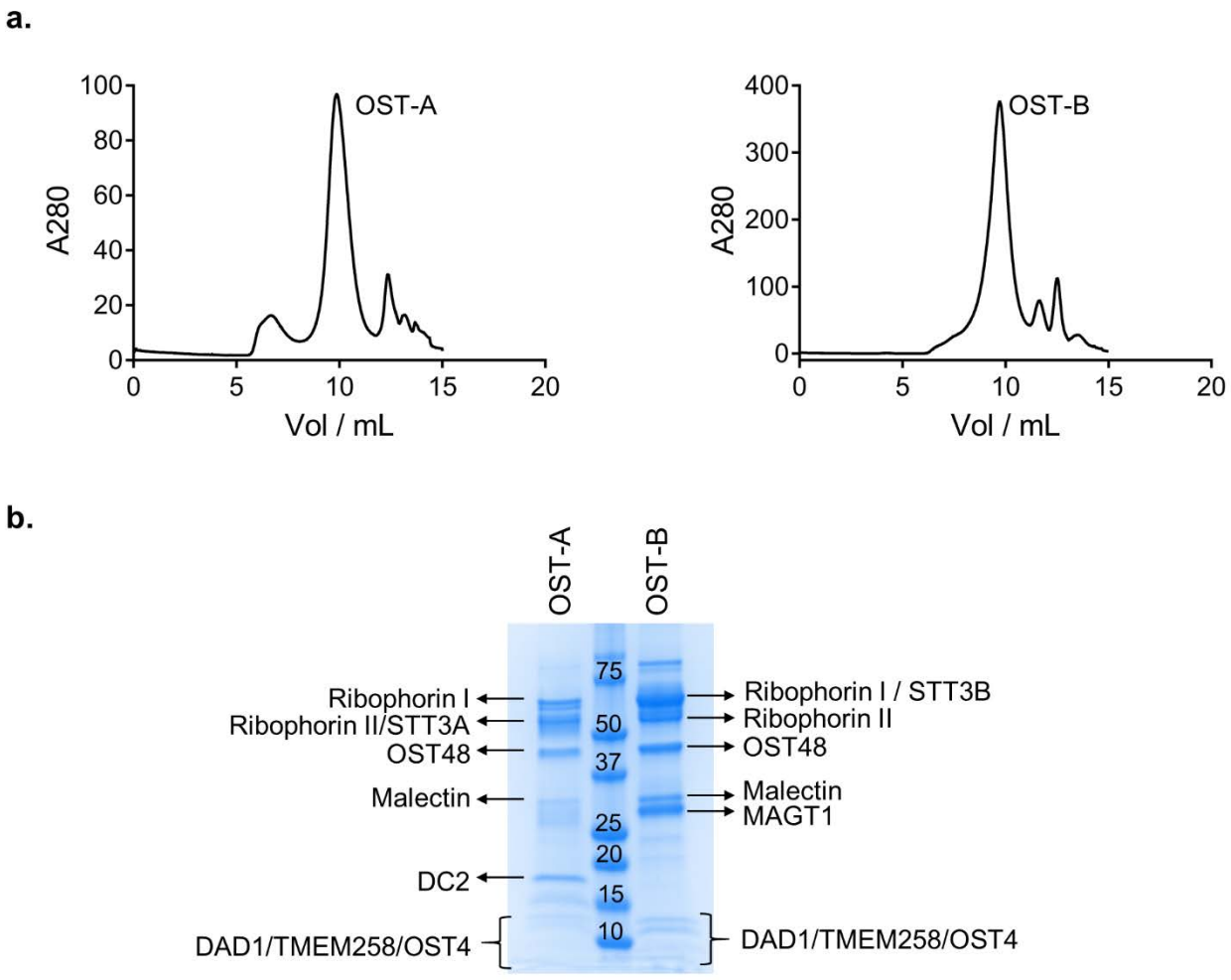

Fig. S1. Purification of OST complexes.

(a) Preparative size exclusion chromatography profiles of purified OST-A (left) and OST-B (right) complexes in a TSK4000XL column. (**b)** SDS-PAGE of purified OST-A and OST-B complexes after preparative SEC.

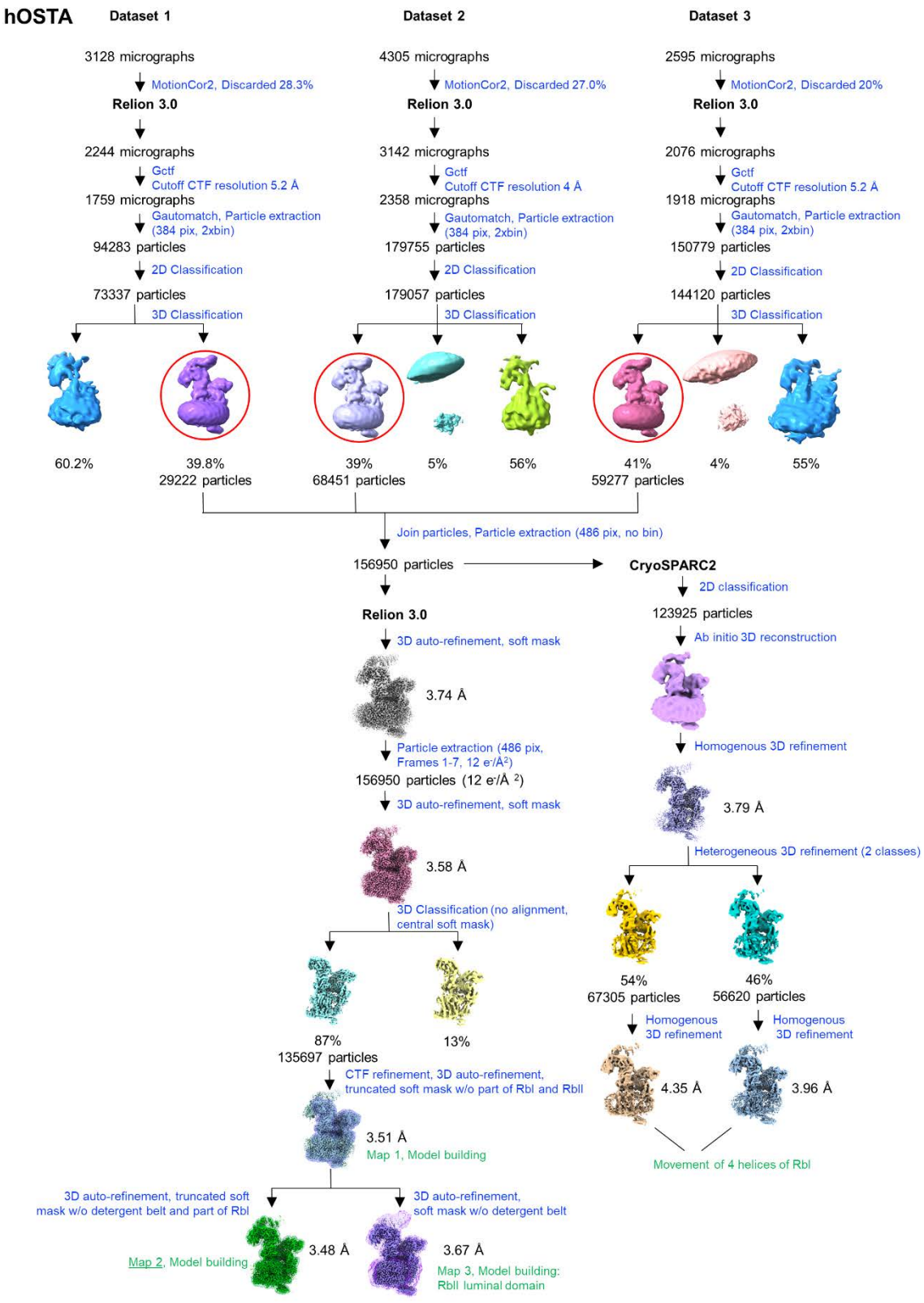

Fig. S2. Cryo-EM data processing of OST-A complex.

Processing of 10,028 EM micrographs from 3 datasets resulted in a total number of 424,817 OST-A particles. After 2D sub-classification most of the particles were kept and subjected to 3D classifications. A final dataset containing 156,950 particles was used for high-resolution 3D refinements within Relion 3.0 and CryoSPARC2 processing pipelines. 3D map quality was gradually improved during further 3D refinements in Relion 3.0 by averaging only the first movie frames 1-7 (~12 e/Å^2), an additional 3D classification without alignments and soft mask refinements for different regions of the complex. Particles were also 2D and 3D classified in CryoSPARC2. Two different conformations of the 4-helix bundle of ribophorin-I were determined.

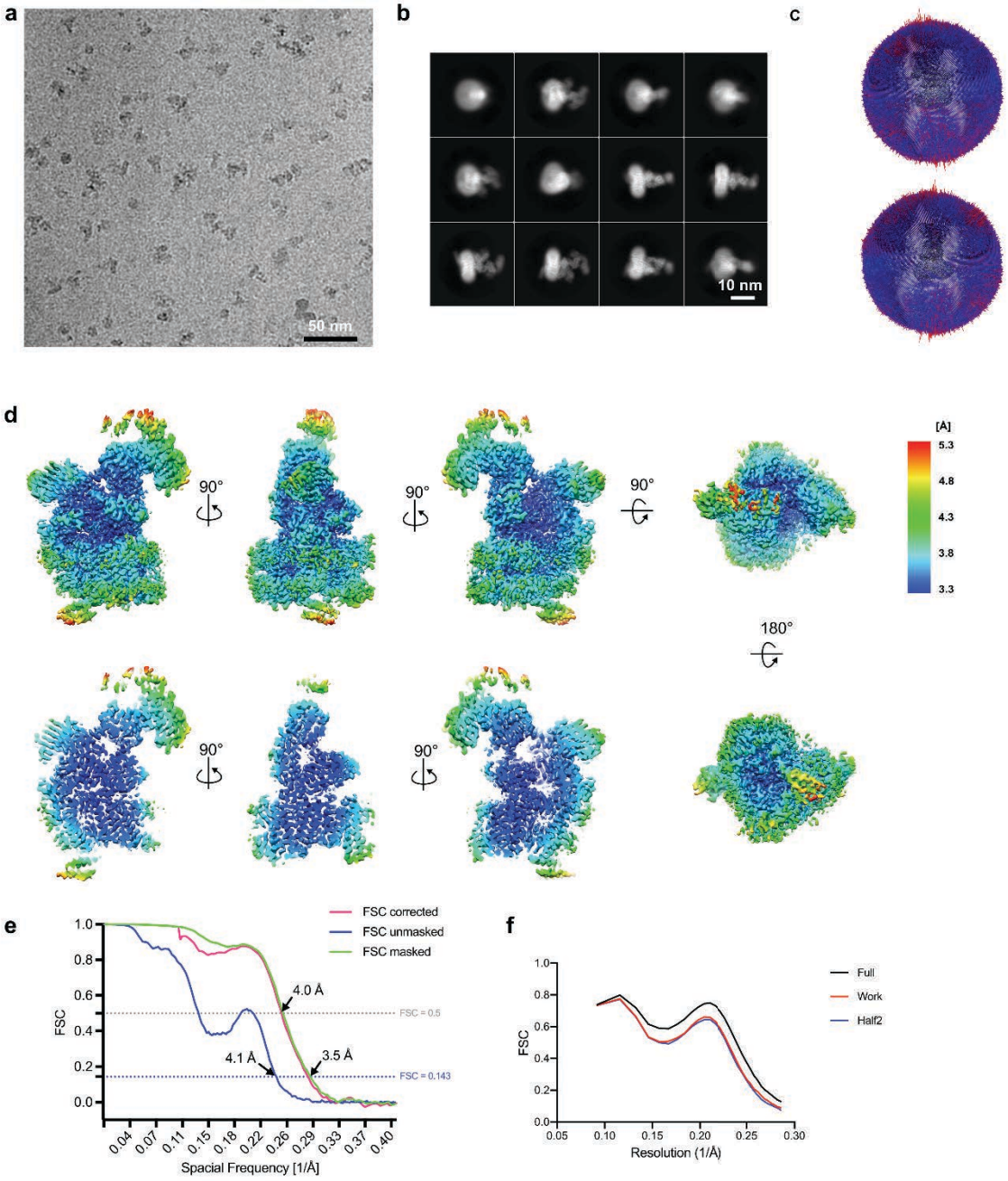

Fig. S3. Cryo-EM map of OST-A generation and resolution estimation.

(a) Exemplary micrograph of purified OST-A after drift correction and dose-weighting. **(b)** Class averages after final round of 2D classification, sorted in descending order by number of particles in each class. **(c)** Angular distribution plot for the final reconstruction from two different views. **(d)** Local resolution of OST-A (Map2, Fig. S2) was determined within Relion 3.0. Coloured full views (upper lane and a last panel in the lower lane) and sliced views (lower lane, first 3 panels) from different orientations illustrate the resolution of different regions in the protein. **(e)** FSC from the Relion 3D autorefine procedure for Map 2 (underlined). Dashed horizontal lines in blue and

grey mark the FSC = 0.143 and FSC = 0.5 criteria, respectively. Deriving map resolutions are indicated. **(f)** FSC curve of the final refined model versus the map against which it was refined (full; black). The FSC curve of the final refined model with introduced shifts (mean value of 0.3 Å) versus the first of two independent half-maps (half-map 1, against which it was refined; work; red) or the same model versus the second independent half-map (against which it was not refined; half2; blue) is also shown.

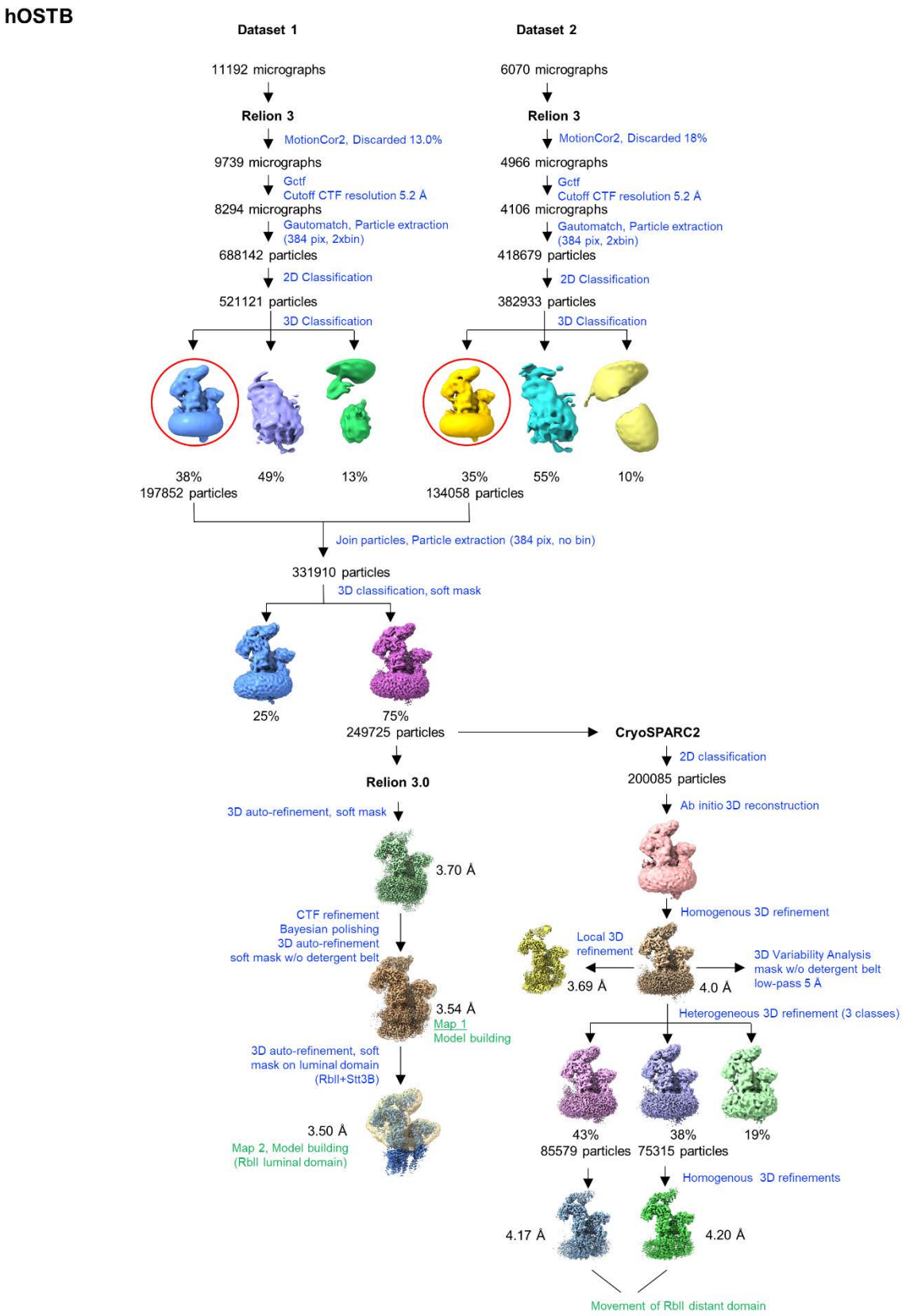

Fig. S4. Cryo-EM data processing of OST-B complex.

Processing of 17,262 EM micrographs from 2 datasets resulted into a total number of 1,106,821 OST-A complex particles. After many rounds of 2D sub-classifications most of the particles were kept and subjected to 3D classifications. A final set of 331,910 was again 3D classified into 2 classes. The best 3D class contained 75% (249,725) of particles and was used for high-resolution soft mask refinements within Relion 3.0 and CryoSPARC2. 3D map quality was gradually improved during further 3D refinements in Relion 3.0 by CTF refinement, Bayesian Polishing and using soft mask refinements for different regions of the complex. In parallel particles were 2D and 3D classified in CryoSPARC2. Two different conformations of the N-terminal domain of ribophorin-II were determined.

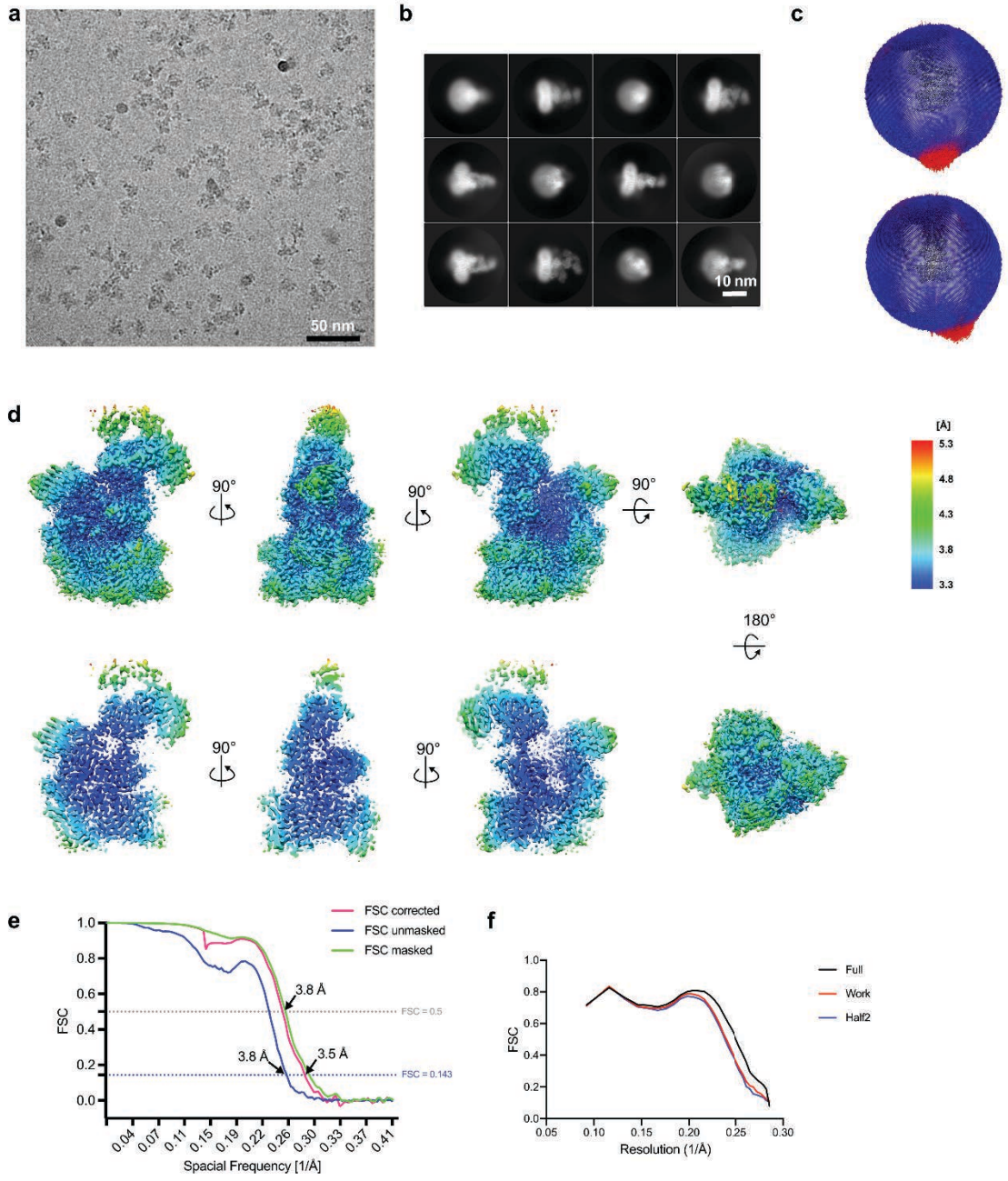

Fig. S5. Cryo-EM map of OST-B generation and resolution estimation.

(a) Exemplary micrograph of purified OST-B after drift correction and dose-weighting. **(b)** Class averages after final round of 2D classification, sorted in descending order by number of particles in each class. **(c)** Angular distribution plot for the final reconstruction from two different views. **(d)** Local resolution of OST-B (Map1, Fig. S4) was determined within Relion 3.0. Coloured full views (upper lane and a last panel in the lower lane) and sliced views (lower lane, first 3 panels) from different orientations illustrate the resolution of different regions in the protein. **(e)** FSC from the Relion 3D autorefine procedure for Map 1 (underlined). Dashed horizontal lines in blue and

grey mark the FSC = 0.143 and FSC = 0.5 criteria, respectively. Deriving map resolutions are indicated. **(f)** FSC curve of the final refined model versus the map against which it was refined (full; black). The FSC curve of the final refined model with introduced shifts (mean value of 0.3 Å) versus the first of two independent half-maps (half-map 1, against which it was refined; work; red) or the same model versus the second independent half-map (against which it was not refined; half2; blue) is also shown.

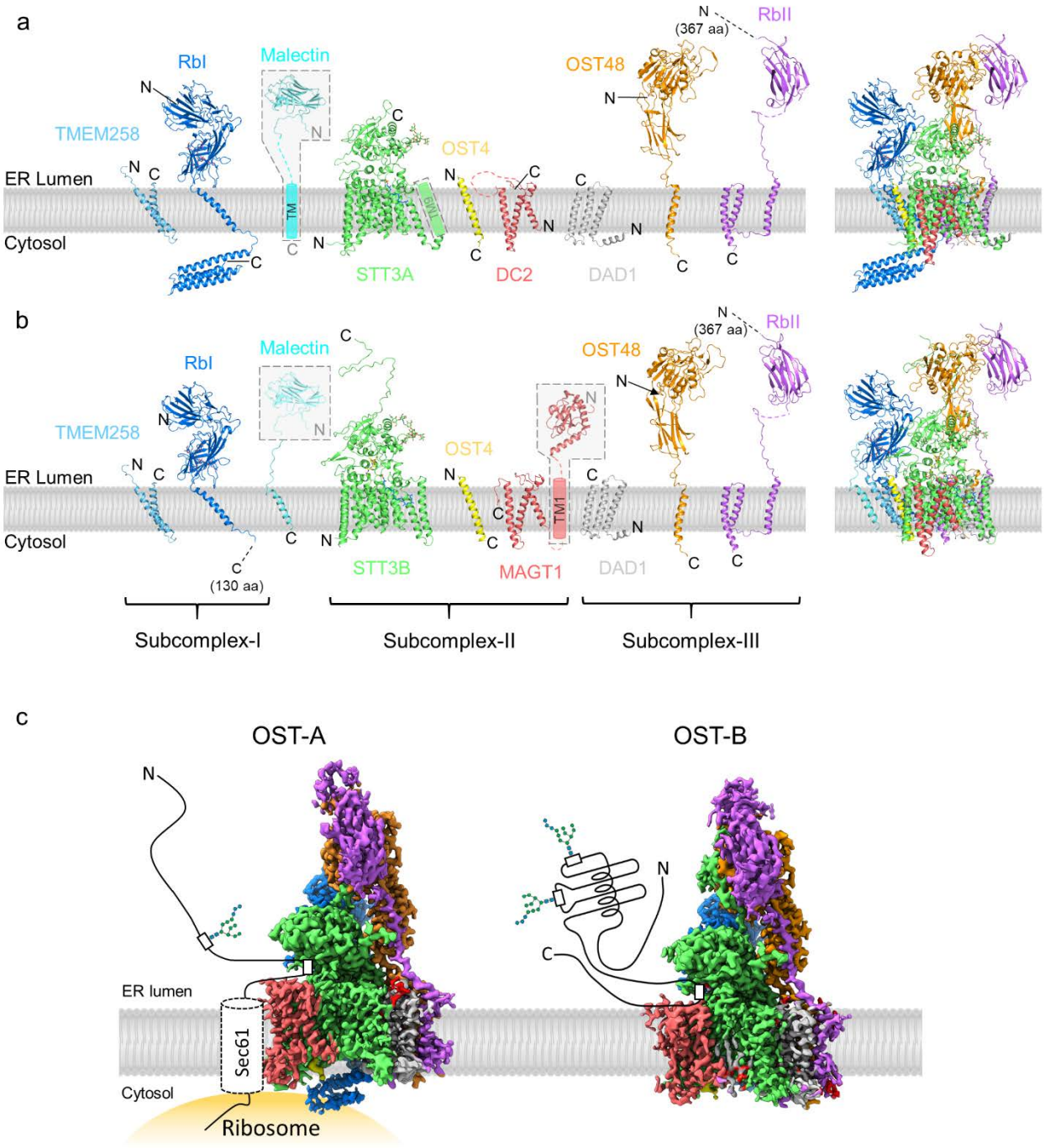

Fig. S6. Architecture, subunit structure and cellular function of human OST-A and OST-B. Structure of individual OST subunits are shown in cartoon representation for **(a)** OST-A and **(b)** OST-B, with subunit names indicated below. On the right side of the panels, the structures of the complete complexes are shown. Ordered *N*-glycans are shown in stick representation. The regions in dashed gray boxes were disordered in the EM maps and are shown schematically. TM9 of STT3A and the single TM of malectin in OST-A, as well as TM1 of MAGT1 in OST-B, are shown as cylinders. The crystal structures of the luminal domain of malectin from *X. laevis* (PDB: 2KR2) and human TUSC3 (PDB: 4M90) are shown in cartoon representation. **(c)** Left: Schematic of co-

translational *N*-glycosylation catalyzed by human OST-A. The cryo-EM map of OST-A is shown and colored according to the subunits as in **(a)**. The translocon component Sec61 is shown as a transparent cylinder and labeled. A bound ribosome is depicted as a yellow surface. Newly synthesized protein is depicted as a black line and glycosylation sequons as white rectangular boxes. Right: Schematic of post-translational N-glycosylation catalyzed by OST-B. The cryo-EM map of OST-B is shown and colored as in **(b)**. Partially folded protein is depicted as a black line and glycosylation sequons as white rectangular boxes.

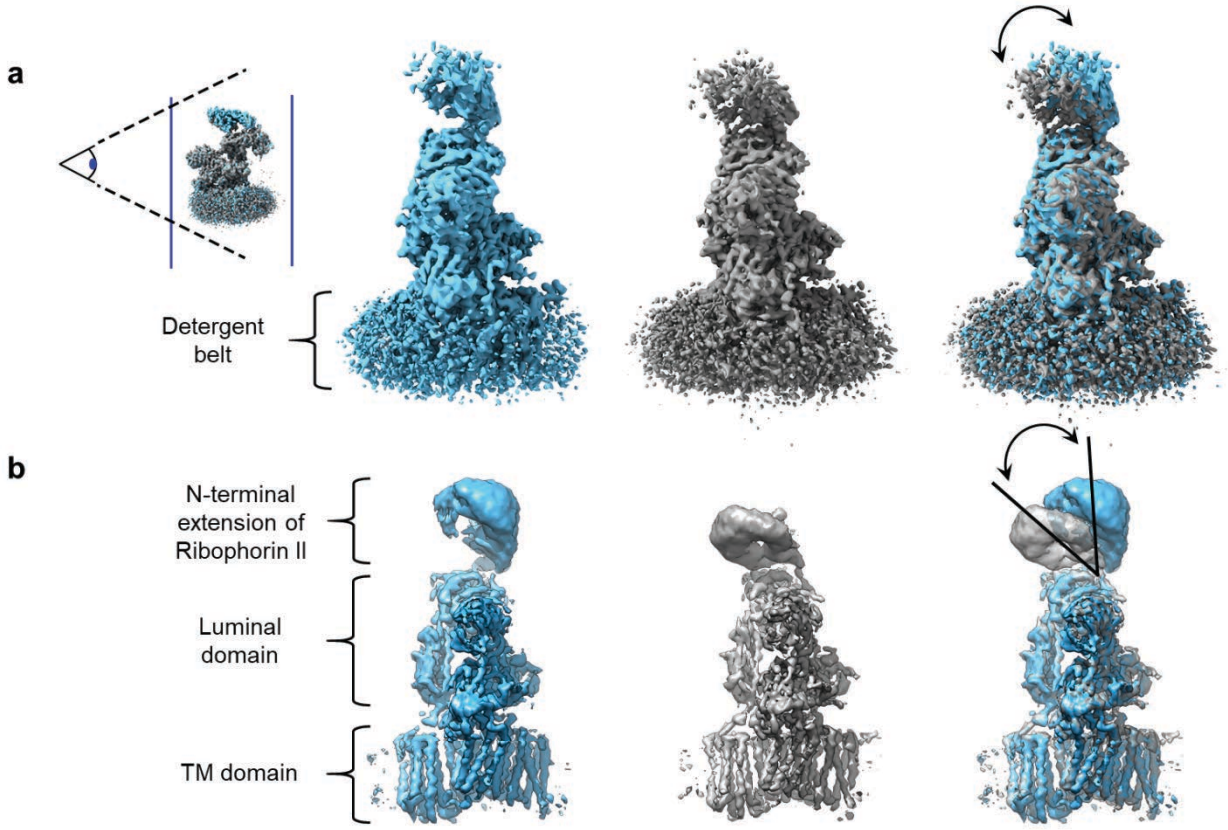

Fig. S7. Different conformations of the N-terminal domain of ribophorin-II in OST-B.

(a) Movement of the N-terminal domain of ribophorin-II in OST-B was analyzed by heterogeneous 3D refinement in CryoSPARC2. Two distinct 3D classes are shown and colored in light blue and grey. The maps are viewed from the membrane plane as indicated. Movement of the N-terminal domain of ribophorin-II is depicted with black arrows. **(b)** 3D Variability Analysis was performed in CryoSPARC 2.9. Two opposite conformations of OST-B (light blue and grey) are shown. An angle of around 45º is marked between the two conformations of the N-terminal domain of ribophorin II. Movement is depicted with black arrows.

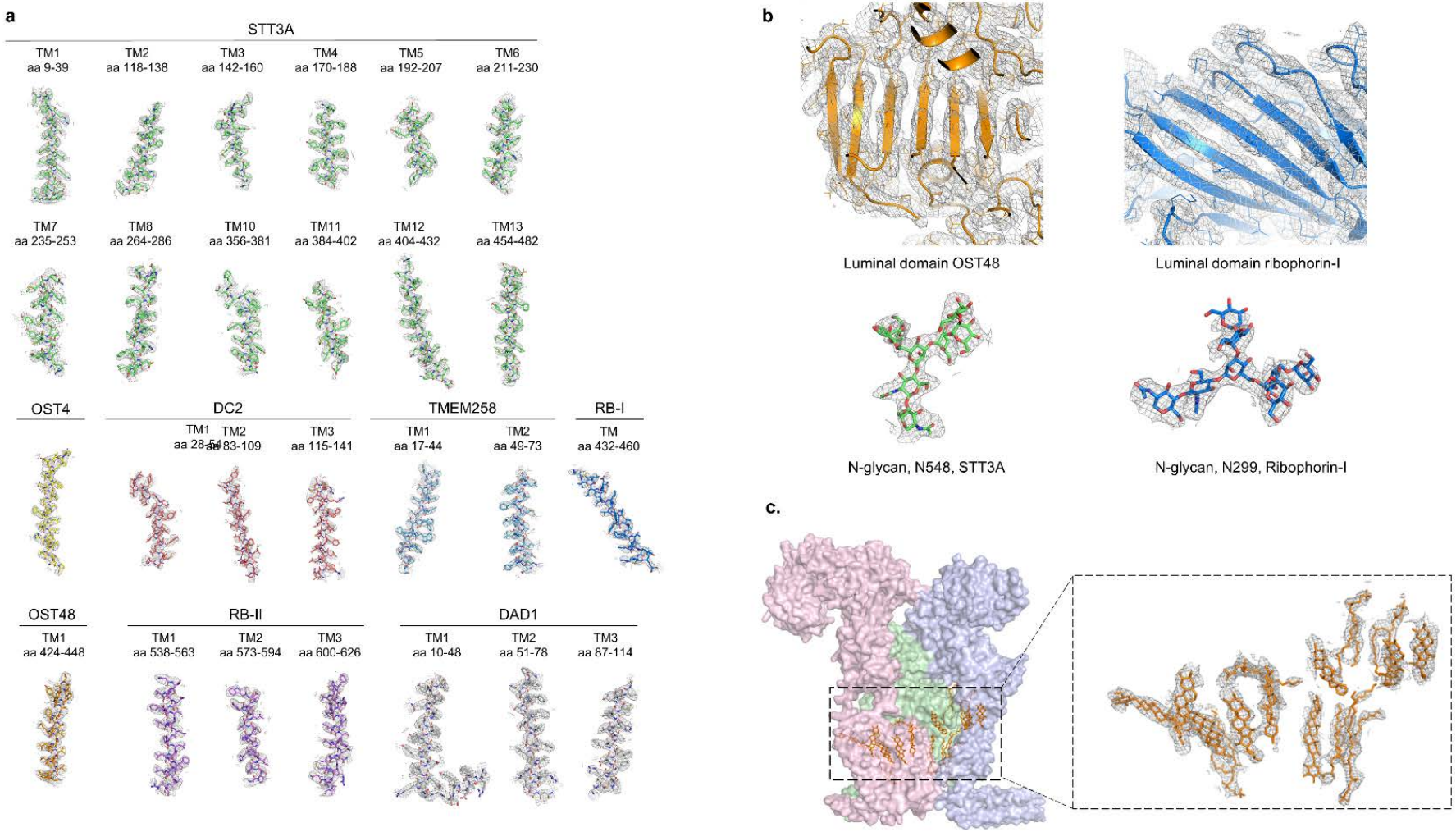

Fig. S8. Fitting of the final OST-A model to the density in the final map.

(a) Fitting of the TM helices of OST-A in the EM density map (Map level: 5.0 σ, as defined by Pymol). A region of up to 3 Å around the atoms is shown. The helices and residues are indicated for each subunit. TM helices and are shown as sticks. Density is shown as a grey mesh. **(b)** Fitting of the luminal regions in the density map, including luminal domains of OST48 and ribophorin-I and two ordered glycans in STT3A and ribophorin-I. **(c)** Fitting of phospholipids and digitonin molecules observed in the OST-A structure.

OST-A is represented as surface, Subcomplex-I is coloured in light purple, Subcomplex-II in light green and Subcomplex-III in light pink. Phospholipids and digitonin molecules are shown as sticks and coloured in orange. Insets show a close view of the molecules of phospholipids and digitonin with their corresponding EM densities shown as a mesh and colored grey.

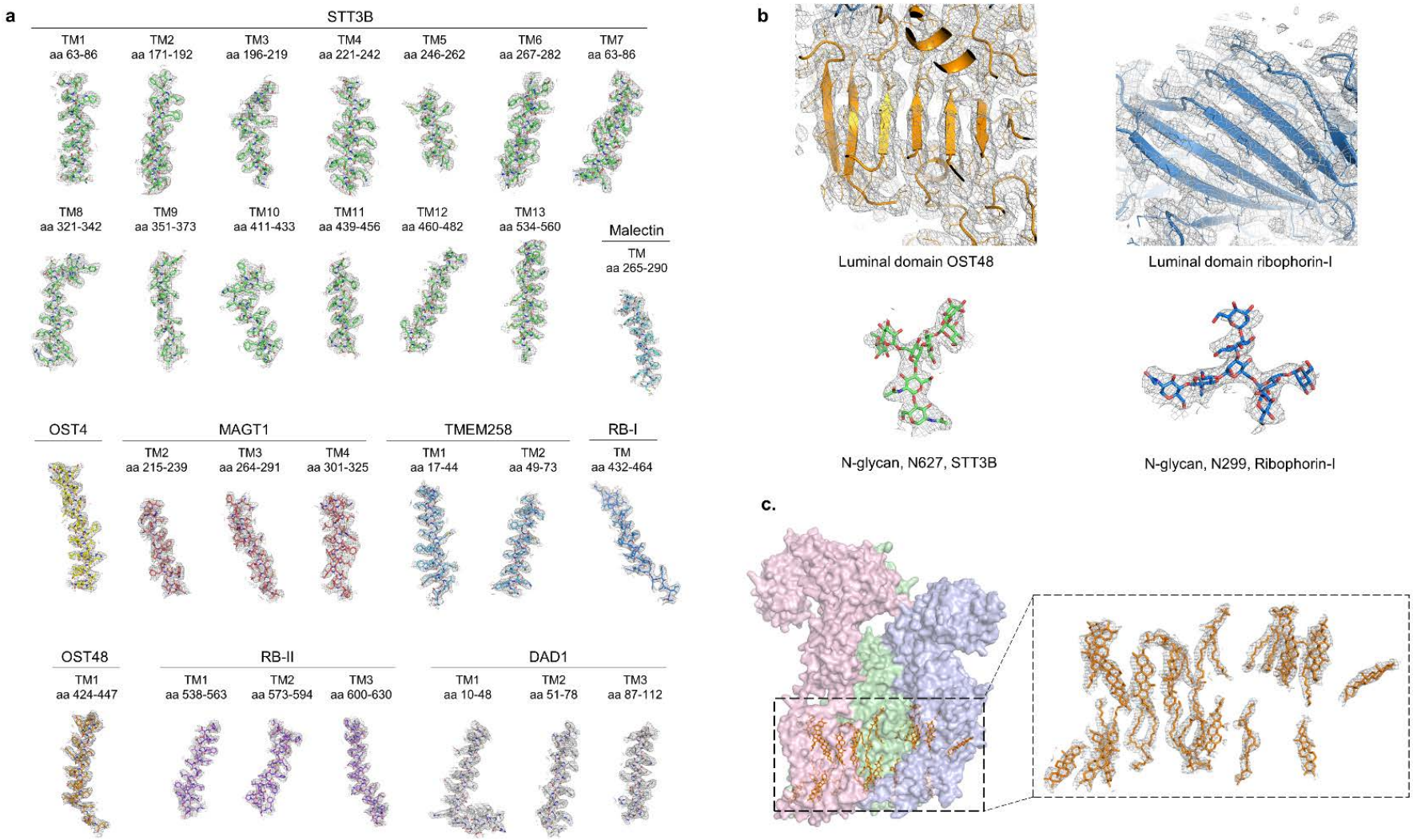

Fig. S9: Fitting of the final OST-B models to the density in the final map.

(a) Fitting of the TM helices of OST-B in the EM density map (Map level: 5.0 σ, as defined by Pymol). A region of up to 3 Å around the atoms is shown. The helices and residues are indicated for each subunit. TM helices and are shown as sticks. Density is shown as

a grey mesh. **(b)** Fitting of the luminal regions in the density map, including luminal domains of OST48 and ribophorin-I and ordered glycans in STT3B and ribophorin-I. **(c)** Fitting of phospholipids and digitonin molecules observed in the OST-B structure. OST-B is represented as surface, Subcomplex-I is coloured in light purple, Subcomplex-II in light green and Subcomplex-III in light pink. Phospholipids and digitonin molecules are shown as sticks and coloured in orange. Insets show a close view of the molecules of phospholipids and digitonin with their corresponding EM density shown as a mesh and colored grey.

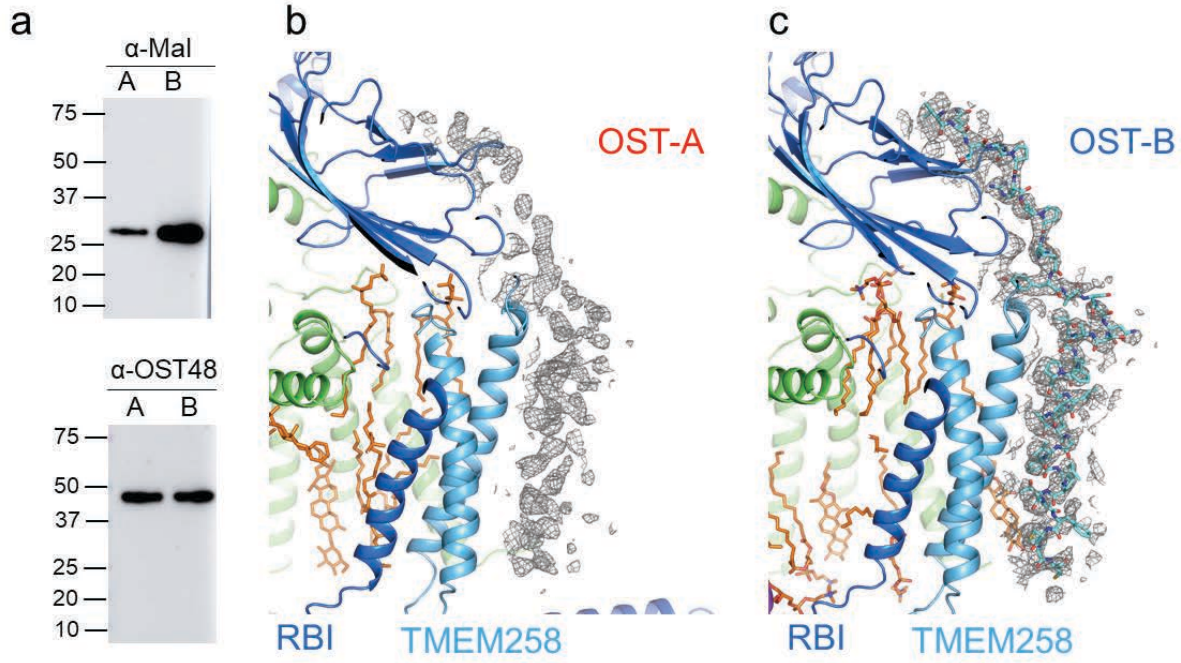

Fig. S10. Malectin bound to human OST-complexes.

(a) Western-blot analysis of purified OST-A and OST-B, using an antibody against malectin (top). The same membrane was stripped and re-probed with an antibody against OST48 (bottom). **(b)** Binding region of malectin in OST-A: TM helices of Subcomplex-I are shown as cartoon and coloured as indicated. Density assigned to malectin in the final map is shown as a grey mesh **(c)** Binding region of malectin in OST-B: TM helices of Subcomplex-I are shown as cartoon and coloured as indicated. Malectin is shown in stick representation. Density assigned to malectin in the final map is shown as a grey mesh. (Map levels: 5.0 σ, as defined by Pymol).

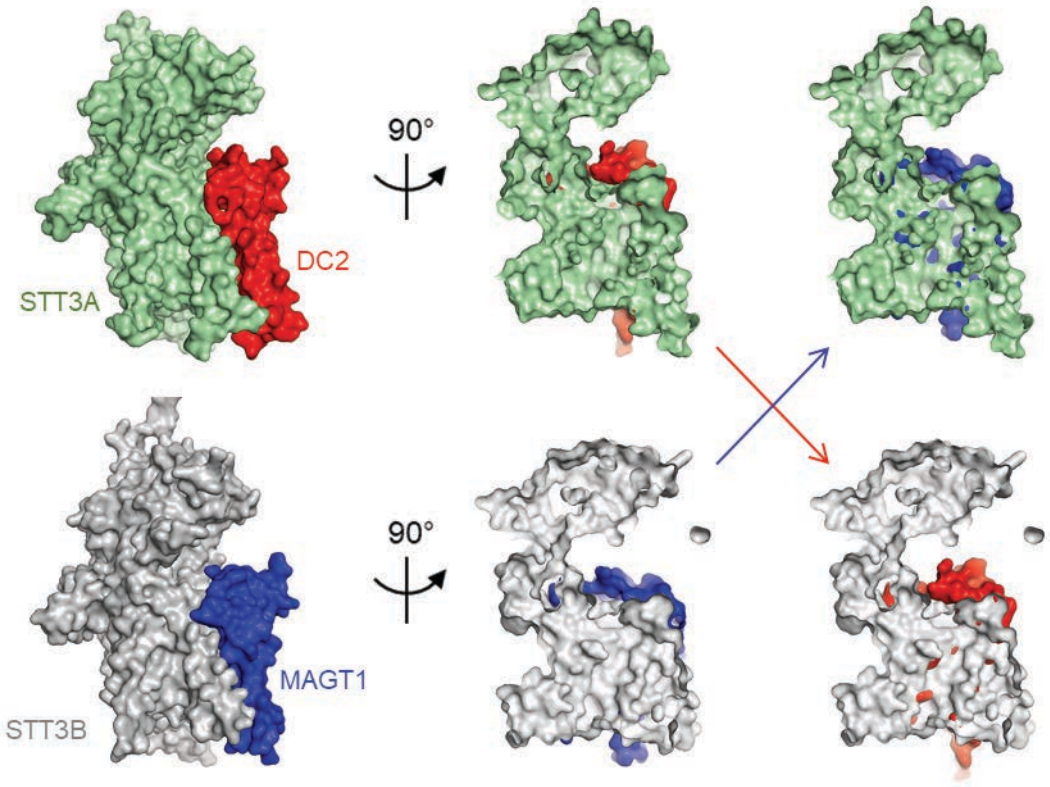

Fig. S11. Analysis of the interaction of STT3 proteins with the adaptor subunits DC2 and MAGT1.

Interaction interface between STT3A-DC2 and STT3B-MAGT1, viewed from within the membrane plane. Proteins are shown in surface representation, labeled and colored as indicated. For each interaction, slices through the surface of the STT3 proteins are shown. Swapping of the STT3 paralogs with their interaction partners has been performed to visualize steric clashes.

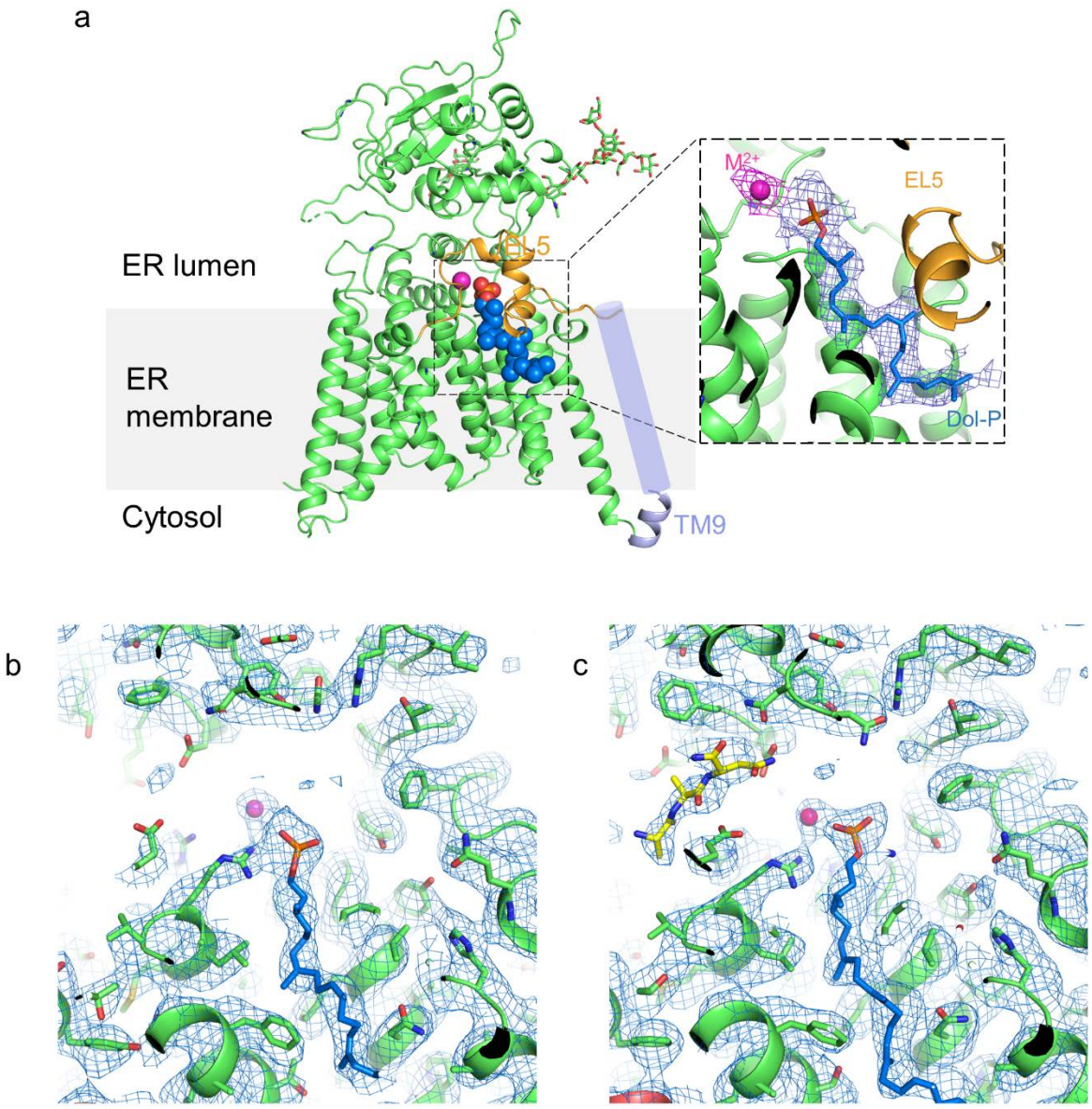

Fig. S12. Comparison of the active site of human OST complexes.

(a) Structure of STT3A shown in cartoon representation. EL5 is colored orange and labeled. Transmembrane helix 9 (TM9) is represented as light blue cylinder and labeled. Close-up of DolP bound to STT3A. DolP is shown as blue sticks and divalent ion as a pink sphere. The EM density around the bound substrates is shown and colored accordingly. **(b)** EM density in the active site of STT3A. STT3A is represented as cartoon with side chains shown as sticks. DolP is shown as sticks colored blue. The metal ion is shown as a pink sphere. The density of the final map is shown as a blue mesh. **(c)** EM density in the active site of STT3B. STT3B is represented as cartoon with side chains shown as sticks. DolP is shown as sticks colored blue. The acceptor substrate is shown as yellow sticks. The metal ion is shown as a pink sphere. The density of the final map is in blue mesh. Map levels: 5.0 σ, as defined by Pymol.

Table S1. Sequence similarity between yeast and human OST subunits.

Yeast OST subunit	Human OST subunit	% Identity	% Similarity
OST1	Ribophorin-I	20.6	35.7
SWP1	Ribophorin-II	10.9 19.3*	19.6 34.0
WBP1	OST48	23.0	40.5
OST2	DAD1	33.0	55.1
OST5	TMEM258	22.7	44.3
OST4	OST4	36.8	55.3
STT3	STT3A STT3B	51.0 47.5	65.7 61.8
OST3	MAGT1	21.9	40.9
OST6	TUSC3	18.6	38.3

*Alignment performed without the first 300 residues of ribophorin-II

Table S2. Cryo-EM data collection, refinement and validation statistics.

Cryo-electron microscopy data collection and processing		
	OST-A	**OST-B**
Microscope	FEI Titan Krios	FEI Titan Krios
Voltage (keV)	300	300
Camera	Gatan K2-Summit	Gatan K2-Summit
Energy Filter	Gatan Quantum-LS (GIF)	Gatan Quantum-LS (GIF)
Pixel size (Å)	0.84	0.84
Defocus range (μm)	(−0.5) - (−2.5)	(−0.5) - (−2.5)
Magnification (nominal)	59,523 (165,000)	59,523 (165,000)
Electron exposure (e^-/pix/s)	6.0	7.0 - 8.0
Exposure rate (e^-/Å^2)	1.7	2.0 – 2.3
Number of frames per movie	40	40
Energy filter slit width (eV)	20	20
Automation Software	Serial EM	EPU
Number of good micrographs	6,035	14,705
Extracted particles	1,106,821	424,817
Particles in final 3D refinement	135,697	249,725
Estimated error of rotations/translations (RELION)	1.127° / 0.695 pix	1.643° / 1.023 pix
Local resolution range (Å)	20 - 3.48	20 – 3.54
Resolution (Å)	3. 48	3.54
Resolution Unmasked 0.143 FSC (Å)	4.1	3.8
Resolution Masked 0.5/0.143 FSC (Å)	4.0 / 3.48	3.8 / 3.54
Sharpening B-factor (Å^2)	−77.8	−133.5
EMDB ID	EMD-10110	EMD-10112
Coordinate refinement and validation		
Refinement program	Phenix (real space)	Phenix (real space)
Number of protein atoms (non-H)	18,121	18,445
Number of ligand atoms (non-H)	599	886
RMSD bonds (Å)	0.005	0.005
RMSD angles (°)	0.729	0.692
Ramachandran favored (%)	94.22	94.24
Ramachandran Allowed (%)	5.60	5.66
Ramachandran Disallowed (%)	0.19	0.09
All-atom clashscore	15.11	10.36
MolProbity Score	2.21	2.23

EMRinger Score	2.98	3.46
Rotamer outliers (%)	1.53	2.55
Cβ outliers (%)	0.00	0.00
CaBLAM outliers (%)	3.35	3.23
B-factors (min/max/mean)		
Protein	3.02/93.31/30.49	9.09/104.87/40.98
Ligand	19.14/112.81/40.17	29.43/98.37/49.61
Overall correlation coefficients		
CC (mask)	0.86	0.86
CC (box)	0.72	0.70
CC (peaks)	0.67	0.66
CC (volume)	0.81	0.82
Mean CC for ligands	0.72	0.73
PDB ID	6S7O	6S7T

Movie S1. Flexibility of the N-terminal domain of ribophorin-II in OST-B complex.